



MIT Open Access Articles

The HERA-19 Commissioning Array: Direction-dependent Effects

The MIT Faculty has made this article openly available. **Please share** how this access benefits you. Your story matters.

As Published	10.3847/1538-4357/AB2F72
Publisher	American Astronomical Society
Version	Final published version
Citable link	https://hdl.handle.net/1721.1/132459
Terms of Use	Article is made available in accordance with the publisher's policy and may be subject to US copyright law. Please refer to the publisher's site for terms of use.



The HERA-19 Commissioning Array: Direction-dependent Effects

Saul A. Kohn¹, James E. Aguirre¹, Paul La Plante¹, Tashalee S. Billings¹, Paul M. Chichura¹, Austin F. Fortino¹, Amy S. Igarashi^{1,2}, Roshan K. Beneto¹, Samavarti Gallardo^{1,3}, Zachary E. Martinot¹, Chuneeta D. Nunhokee^{1,4,5}, Nicholas S. Kern⁵, Philip Bull⁶, Adrian Liu^{5,7}, Paul Alexander⁸, Zaki S. Ali⁵, Adam P. Beardsley^{1,9}, Gianni Bernardi^{4,10,11}, Judd D. Bowman⁹, Richard F. Bradley¹², Chris L. Carilli^{8,13}, Carina Cheng⁵, David R. DeBoer⁵, Eloy de Lera Acedo⁸, Joshua S. Dillon^{5,27}, Aaron Ewall-Wice^{14,15}, Gcobisa Fadana¹⁶, Nicolas Fagnoni⁸, Randall Fritz¹⁶, Steven R. Furlanetto¹⁷, Brian Glendenning¹³, Bradley Greig^{18,19}, Jasper Grobbelaar¹¹, Bryna J. Hazelton^{20,21}, Jacqueline N. Hewitt²², Jack Hickish⁵, Daniel C. Jacobs⁹, Austin Julius¹¹, MacCalvin Kariseb¹¹, Matthew Kolopanis⁹, Telalo Lekalake¹¹, Anita Loots¹¹, David MacMahon⁵, Lourence Malan¹¹, Cresshim Malgas¹¹, Matthys Maree¹¹, Nathan Mathison¹¹, Eunice Matsetela¹¹, Andrei Mesinger²³, Miguel F. Morales²⁰, Abraham R. Neben²², Bojan Nikolic⁸, Aaron R. Parsons⁵, Nipanjana Patra⁵, Samantha Pieterse¹¹, Jonathan C. Pober²⁴, Nima Razavi-Ghods⁸, Jon Ringuette²⁰, James Robnett¹³, Kathryn Rosie¹¹, Raddwine Sell¹¹, Craig Smith¹¹, Angelo Syce¹¹, Max Tegmark²², Nithyanandan Thyagarajan^{9,13,28}, Peter K. G. Williams^{25,26}, and Haoxuan Zheng²²

¹ Department of Physics and Astronomy, University of Pennsylvania, Philadelphia, PA 19104, USA; jaguirre@sas.upenn.edu

² Department of Astronomy, San Diego State University, San Diego, CA 92182, USA

³ California State University of Los Angeles, 5151 State University Drive, Los Angeles, CA 90032, USA

⁴ Department of Physics and Electronics, Rhodes University, PO Box 94, Grahamstown 6140, South Africa

⁵ Department of Astronomy, University of California, Berkeley, CA, USA

⁶ School of Physics & Astronomy, Queen Mary University of London, Mile End Road, London E1 4NS, UK

⁷ Department of Physics and McGill Space Institute, McGill University, 3600 University Street, Montreal, QC H3A 2T8, Canada

⁸ Cavendish Astrophysics, University of Cambridge, Cambridge, UK

⁹ School of Earth and Space Exploration, Arizona State University, Tempe, AZ, USA

¹⁰ INAF-Istituto di Radioastronomia, via Gobetti 101, I-40129 Bologna, Italy

¹¹ SKA SA, 3rd Floor, The Park, Park Road, Pinelands 7405, South Africa

¹² National Radio Astronomy Observatory, Charlottesville, VA, USA

¹³ National Radio Astronomy Observatory, Socorro, NM, USA

¹⁴ Jet Propulsion Laboratory, 4800 Oak Grove Drive, Pasadena, CA, USA

¹⁵ Dunlap Institute for Astronomy and Astrophysics, Toronto, Ontario, Canada

¹⁶ SKA-SA, Cape Town, South Africa

¹⁷ Department of Physics and Astronomy, University of California, Los Angeles, CA, USA

¹⁸ ARC Centre of Excellence for All-Sky Astrophysics in 3 Dimensions (ASTRO 3D), University of Melbourne, VIC 3010, Australia

¹⁹ School of Physics, University of Melbourne, Parkville, VIC 3010, Australia

²⁰ Department of Physics, University of Washington, Seattle, WA, USA

²¹ eScience Institute, University of Washington, Seattle, WA, USA

²² Department of Physics, Massachusetts Institute of Technology, Cambridge, MA, USA

²³ Scuola Normale Superiore, Pisa, Italy

²⁴ Department of Physics, Brown University, Providence, RI, USA

²⁵ American Astronomical Society, Washington, DC 20006 USA

²⁶ Center for Astrophysics—Harvard & Smithsonian, Cambridge, MA 02138 USA

Received 2018 February 7; revised 2019 June 29; accepted 2019 July 3; published 2019 September 2

Abstract

Foreground power dominates the measurements of interferometers that seek a statistical detection of highly-redshifted H I emission from the Epoch of Reionization (EoR). The chromaticity of the instrument creates a boundary in the Fourier transform of frequency (proportional to k_{\parallel}) between spectrally smooth emission, characteristic of the strong synchrotron foreground (the “wedge”), and the spectrally structured emission from H I in the EoR (the “EoR window”). Faraday rotation can inject spectral structure into otherwise smooth polarized foreground emission, which through instrument effects or miscalibration could possibly pollute the EoR window. For instruments pursuing a “foreground avoidance” strategy of simply measuring in the EoR window, and not attempting to model and remove foregrounds, as is the plan for the first stage of the Hydrogen Epoch of Reionization Array (HERA), characterizing the intrinsic instrument polarization response is particularly important. Using data from the HERA 19-element commissioning array, we investigate the polarization response of this new instrument in the power-spectrum domain. We perform a simple image-based calibration based on the unpolarized diffuse emission of the Global Sky Model, and show that it achieves qualitative redundancy between the nominally redundant baselines of the array and reasonable amplitude accuracy. We construct power spectra of all fully polarized coherencies in all pseudo-Stokes parameters, and discuss the achieved isolation of foreground power due to the intrinsic spectral smoothness of the foregrounds, the instrument chromaticity, and the calibration. We compare to simulations based on an unpolarized diffuse sky model and detailed electromagnetic simulations of the dish and feed, confirming that in Stokes I , the calibration does not add significant spectral structure beyond that expected from the interferometer array configuration and the modeled primary beam response. Furthermore, this calibration is stable over the 8 days of

²⁷ NSF Astronomy and Astrophysics Postdoctoral Fellow.

²⁸ Jansky Fellow.

observations considered. Excess power is seen in the power spectra of the linear polarization Stokes parameters, which is not easily attributable to leakage via the primary beam, and results from some combination of residual calibration errors and actual polarized emission. Stokes V is found to be highly discrepant from the expectation of zero power, strongly pointing to the need for more accurate polarized calibration.

Key words: cosmology: observations – dark ages, reionization, first stars – instrumentation: interferometers – polarization – techniques: interferometric

1. Introduction

Many low-frequency (50–200 MHz) radio interferometers (e.g., LOFAR,²⁹ MWA,³⁰ PAPER,³¹ Hydrogen Epoch of Reionization Array (HERA)³²) around the world are seeking to detect brightness-temperature fluctuations of neutral hydrogen during the Epoch of Reionization (EoR; for an overview see Furlanetto et al. 2006). Such a detection is predicted to be rich in information about the astrophysics and cosmology of the high-redshift ($\sim 7 < z < 14$) universe. The HI brightness-temperature fluctuations are not only intrinsically faint but also hidden by foreground emission. Foreground emission, predominantly in the form of galactic and extragalactic synchrotron emission, is many orders of magnitude more powerful than the cosmological signal (e.g., Bernardi et al. 2009; Pober et al. 2013; Dillon et al. 2014).

Most foreground emission is due to synchrotron emission, which is spectrally smooth. The instrumental response of an interferometer is inherently chromatic, and the cosmological signal is spectrally structured. In sum, this leads to the property that Fourier transforming the interferometric measurement along the frequency axis delineates a boundary in the \mathbf{k} -space between the spectrally smooth foregrounds (in the “wedge”) and the cosmological HI signal (in the “EoR window”) (Datta et al. 2010; Morales et al. 2012; Parsons et al. 2012a, 2012b; Trott et al. 2012; Vedantham et al. 2012; Pober et al. 2013, 2014; Thyagarajan et al. 2013; Liu et al. 2014a, 2014b; Dillon et al. 2015b, 2015a; Thyagarajan et al. 2015a, 2015b). Thermal noise is present throughout this space, and dominates the EoR window in any single observation. Detection of the EoR thus requires long observing seasons, precision calibration, and suppression of instrument systematics.

The cosmological HI signal is strongly unpolarized (Mishra & Hirata 2018). However, polarized synchrotron radiation represents a potential foreground contaminant capable of leaking into the EoR window. At low frequencies, Faraday rotation can impart significant spectral structure to polarized emission (e.g., Moore et al. 2013). This polarized signal is able to “leak” into unpolarized measurements due to miscalibration and instrumental effects (Carozzi & Woan 2009; Geil et al. 2011; Moore et al. 2013; Asad et al. 2015, 2016; Kohn et al. 2016; Nunhokee et al. 2017), contaminating the EoR window.

It is important to constrain intrinsic and leaked polarized signal for any HI intensity mapping experiment. The objective of this paper is an exploration of eight nights of data from the HERA 19-element commissioning array, coupled with simulations of the instrument, in order to characterize the polarized response of this interferometer. One of the more difficult features of an interferometer to characterize is the frequency- and direction-dependent polarized antenna response, which is

important for characterizing polarized-to-unpolarized leakage in the wedge/window paradigm (Moore et al. 2017; Nunhokee et al. 2017; Martinot et al. 2018). In this work, we were primarily sensitive to leakage in the unpolarized-to-polarized direction. Due to the symmetry of leakage modes (elaborated upon in Section 2), this still represents a useful constraint on the future problem of polarized-to-unpolarized leakage contaminating the EoR signal. While we use cosmological power spectra as a diagnostic of the data, the goal of this paper is not to obtain new upper limits on the EoR power spectrum, but simply to integrate deep enough to test models of the instrument’s spectral response against simulations.

This work is organized as follows. In Section 2 we review the theory behind polarization leakage into unpolarized signal and present the polarized primary beam model for the HERA commissioning array. In Section 3 we describe the HERA data that we used, its calibration, and reduction to power spectra. We present our results and discuss the implications in Section 4, then conclude in Section 5.

We assume the cosmological parameters reported by Planck Collaboration et al. (2016) throughout.

2. Leakage Modes

A radio interferometer measures correlations of voltages. Viewed in transmission, a dipole arm of antenna i radiates a far-field electric field pattern

$$E_i(\hat{s}, \nu) = E_{i,\theta}(\nu)\hat{\theta} + E_{i,\phi}(\nu)\hat{\phi}, \quad (1)$$

where $(\hat{\theta}, \hat{\phi})$ define an orthogonal coordinate system on the sphere. These far-field beam patterns, by the reciprocity theorem, define the response of the feed to an electric field from infinity in the direction (θ, ϕ) .

We may choose to express the electric field response in a R.A. and decl. basis (unit vectors $\hat{e}_\alpha, \hat{e}_\delta$), allowing us to express the coherency tensor field

$$\begin{aligned} C = & \langle E_\delta^* E_\delta \rangle \hat{e}_\delta \otimes \hat{e}_\delta + \langle E_\alpha^* E_\delta \rangle \hat{e}_\alpha \otimes \hat{e}_\delta \\ & + \langle E_\delta^* E_\alpha \rangle \hat{e}_\delta \otimes \hat{e}_\alpha + \langle E_\alpha^* E_\alpha \rangle \hat{e}_\alpha \otimes \hat{e}_\alpha, \end{aligned} \quad (2)$$

where we have dropped the explicit (\hat{s}, ν) dependence of the fields. By definition, the coherency field is specified by the Stokes parameters

$$C = \begin{pmatrix} I(\hat{s}, \nu) + Q(\hat{s}, \nu) & U(\hat{s}, \nu) - iV(\hat{s}, \nu) \\ U(\hat{s}, \nu) + iV(\hat{s}, \nu) & I(\hat{s}, \nu) - Q(\hat{s}, \nu) \end{pmatrix}. \quad (3)$$

Each polarized feed p of antenna i responds to incident radiation from direction $(\hat{\theta}, \hat{\phi})$ with a complex vector antenna pattern

$$\vec{A}_i^p(\hat{s}, \nu) = A_{i,\theta}^p(\hat{s}, \nu)\hat{\theta} + A_{i,\phi}^p(\hat{s}, \nu)\hat{\phi}. \quad (4)$$

The antenna patterns can be written as components of a direction-dependent Jones matrix for a dipole feed i with arms

²⁹ www.lofar.org

³⁰ www.mwatelescope.org

³¹ eor.berkeley.edu

³² www.reionization.org

p and q :

$$\mathcal{J}_i = \begin{pmatrix} A_{i,\theta}^p(\hat{s}, \nu) & A_{i,\phi}^p(\hat{s}, \nu) \\ A_{i,\theta}^q(\hat{s}, \nu) & A_{i,\phi}^q(\hat{s}, \nu) \end{pmatrix}. \quad (5)$$

We can then express the fully polarized visibility equation for the correlation of feeds i and j as

$$\mathcal{V}_{ij} = \int \mathcal{J}_i \mathcal{J}_j^\dagger \exp(-2\pi i \mathbf{b} \cdot \hat{s}/c) d\Omega = \begin{pmatrix} V_{ij}^{nn} & V_{ij}^{ne} \\ V_{ij}^{en} & V_{ij}^{ee} \end{pmatrix}, \quad (6)$$

where we have denoted dipole arms p and q as n and e , representing a configuration where the arms are oriented along the north–south and east–west directions, respectively.

Unless \mathcal{J} is both diagonal and has, at any given point on the sphere, equal diagonal elements, there will be mixing or “leaking” of different Stokes parameters together into each element of \mathcal{V} in a direction-dependent way (Geil et al. 2011; Smirnov 2011a, 2011b; Nunhokee et al. 2017).

2.1. Direction-dependent Leakage

The cosmological signal of interest for 21 cm cosmology studies is effectively unpolarized, and we therefore use the pseudo-Stokes³³ I visibility to measure it (e.g., Moore et al. 2013); this is defined $V^I = V^{nn} + V^{ee}$, which is the trace of \mathcal{V} :

$$\begin{aligned} V_{ij}^I(\nu) &= \text{Tr}(\mathcal{V}_{ij}) = \int \text{Tr}(\mathcal{J}_i \mathcal{J}_j^\dagger) \exp(-2\pi i \mathbf{b} \cdot \hat{s}/c) d\Omega \\ &= \int (\mathcal{M}_{00}I + \mathcal{M}_{01}Q + \mathcal{M}_{02}U + \mathcal{M}_{03}V) \\ &\quad \times \exp(-2\pi i \mathbf{b} \cdot \hat{s}/c) d\Omega, \end{aligned} \quad (7)$$

where I , Q , U , and V are the true Stokes sky and are functions of direction and frequency, and $\mathcal{M}_{ab}(\hat{s}, \nu)$ are the instrumental Mueller matrix elements:

$$\mathcal{M}_{ab}(\hat{s}, \nu) = \text{Tr}(\sigma_a \mathcal{J}_b \mathcal{J}^\dagger) \quad (8)$$

and σ_i are the Pauli matrices (where the indices are reordered from the quantum mechanical convention to an order that gives the ordering of the Stokes vector as (I, Q, U, V) ; see, e.g., Shaw et al. 2015).

We simulated the HERA feed, faceted parabolic dish, and analog signal chain using CST³⁴ to generate the complex \mathbf{E} -field receptivity patterns, as described in Fagnoni & de Lera Acedo (2016; also see public HERA Memo #21³⁵), and then formed \mathcal{J} and \mathcal{M} as described above. Examples of \mathcal{M}_{ij} at 120 MHz and 160 MHz (our low and high bands of interest; see Section 3.2) are shown in Figure 1, projected in the R.A./decl. basis. Note that this basis has a singularity at the South Pole, leading to wide-field asymmetries in Q and U . Due to the large spread in dynamic ranges between \mathcal{M}_{00} , other diagonal terms, and off-diagonal terms, we use separate color maps for each. All of the dynamic ranges are normalized to the peak of \mathcal{M}_{00} , which is 1 at zenith. The off-diagonal terms are 2–8 orders of magnitude less than the diagonal terms.

The key for these matrices are the mappings of Stokes parameters into pseudo-Stokes visibilities, following

$$\mathcal{M}_{ab}(\hat{s}, \nu) = \begin{pmatrix} I \rightarrow V^I & I \rightarrow V^Q & I \rightarrow V^U & I \rightarrow V^V \\ Q \rightarrow V^I & Q \rightarrow V^Q & Q \rightarrow V^U & Q \rightarrow V^V \\ U \rightarrow V^I & U \rightarrow V^Q & U \rightarrow V^U & U \rightarrow V^V \\ V \rightarrow V^I & V \rightarrow V^Q & V \rightarrow V^U & V \rightarrow V^V \end{pmatrix}, \quad (9)$$

where pseudo-Stokes visibilities are formed as

$$\begin{pmatrix} V^I \\ V^Q \\ V^U \\ V^V \end{pmatrix} = \frac{1}{2} \begin{pmatrix} 1 & 0 & 0 & 1 \\ 1 & 0 & 0 & -1 \\ 0 & 1 & 1 & 0 \\ 0 & -i & i & 0 \end{pmatrix} \begin{pmatrix} V^{nn} \\ V^{ne} \\ V^{en} \\ V^{ee} \end{pmatrix}. \quad (10)$$

At low frequencies and the large scales probed by many low-frequency interferometers, Stokes I is extremely bright compared to the other Stokes parameters (Bernardi et al. 2009, 2010; Jelić et al. 2014, 2015; Asad et al. 2015; Kohn et al. 2016; Lenc et al. 2017; Moore et al. 2017). Moreover, only a few polarized point sources have been observed at frequencies below 300 MHz (Bernardi et al. 2013; Asad et al. 2016; Lenc et al. 2017). Farnes et al. (2014) showed evidence for systematic depolarization of steep-spectrum point sources toward low frequencies, causing low polarization fractions ($\ll 1\%$) below 300 MHz.

The “linear polarization leakage beam” is shown for the two central frequencies of this analysis in Figure 2. This quantity is the magnitude of the spin-2 function $\mathcal{M}_{IQ} + i\mathcal{M}_{IU}$ and represents the amplitude of the direction-dependent leakage of Stokes Q and U into I .

These factors make the first row of \mathcal{M} , which represents $I \rightarrow V^I, V^Q, V^U, V^V$, the most interesting for low-frequency polarized power spectra, as with limited calibration we can expect leakage from Stokes I into the other Stokes parameters to dominate over Stokes Q , U , and V emission alone.

We produced simulations \mathcal{V} using our fully polarized formalism for the HERA-19 commissioning array, described below, using an unpolarized model of the low-frequency sky from the Global Sky Model (GSM; de Oliveira-Costa et al. 2008; Price 2016; Zheng et al. 2017) at the appropriate R.A. range to match our observations. These simulations are based on the same source code as Martinot et al. (2018).

Forming power spectra from these visibilities allowed for a comparison of our data to a “leakage only” regime. We discuss the process for forming power spectra in Section 3.3, and the simulated power spectra are shown in comparison to those from data in Section 4.

2.2. Direction-independent Leakage

In addition to the mixing of Stokes parameters due to the primary beam, it is possible to mix them in a direction-independent way. Calibration errors are capable of leaking signal between pseudo-Stokes visibilities independent of the sky (Thompson et al. 2008). Again focusing on the $\{V^I, V^Q, V^U, V^V\}$ components of this leakage, we have:

1. $V^I \rightarrow V^Q$ occurs through errors in calibrating the complex voltage gain factors for each dipole arm.
2. $V^I \rightarrow V^U$ occurs through the sum of off-diagonal gain terms (D -terms; the receptivity of dipole arm “n” to an electric field vector aligned with arm “e” and vice versa).

³³ We use “pseudo-Stokes” to refer to Stokes parameters formed from visibilities throughout this work, to distinguish from “true” Stokes parameters defined in the image domain by the IEEE (Ludwig 1973; van Straten et al. 2010).

³⁴ www.cst.com

³⁵ http://reionization.org/wp-content/uploads/2013/03/HERA_memo_21_CST_simulation_of_HERA_and_comparison_with_measurements.pdf

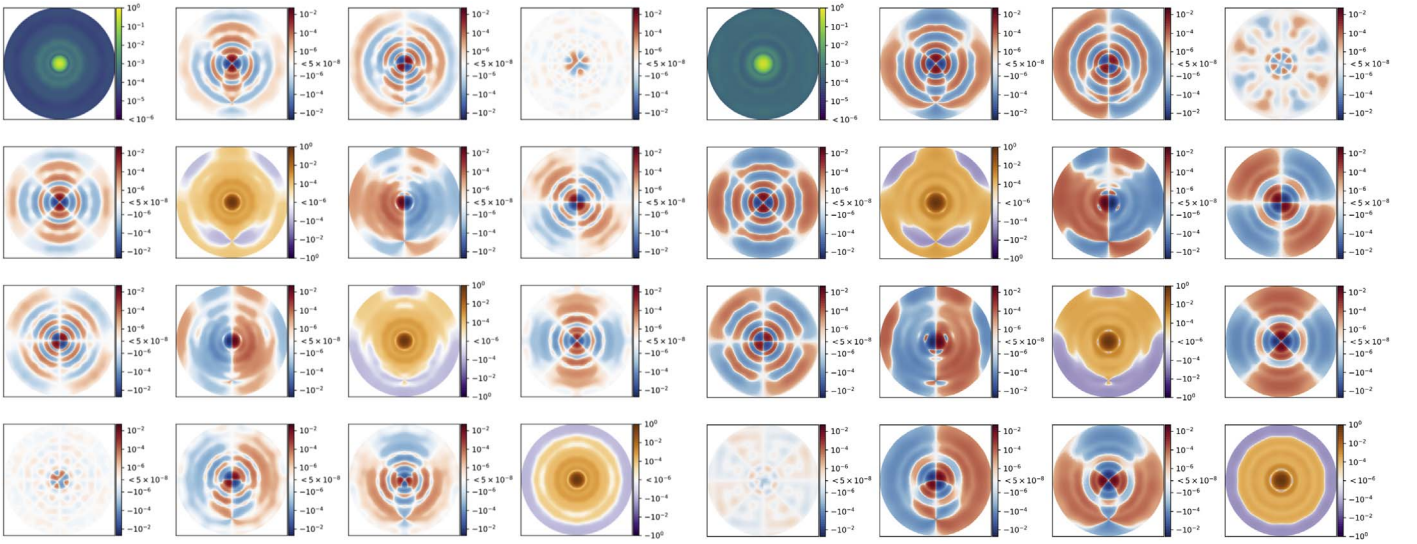


Figure 1. Simulations of the instrumental direction-dependent Mueller matrix at 120 MHz and 160 MHz (above and below, respectively) projected into the R.A., decl. basis. Color scales for frequencies are relative to the peak of \mathcal{M}_{00} (which itself is normalized to 1 at zenith). To account for the wide variety of dynamic ranges required to show detail, we use separate color maps for \mathcal{M}_{00} , diagonal, and off-diagonal terms. The off-diagonal terms are 2 to 8 orders of magnitude less than the diagonal terms. For a key to these matrices, see Equation (9).

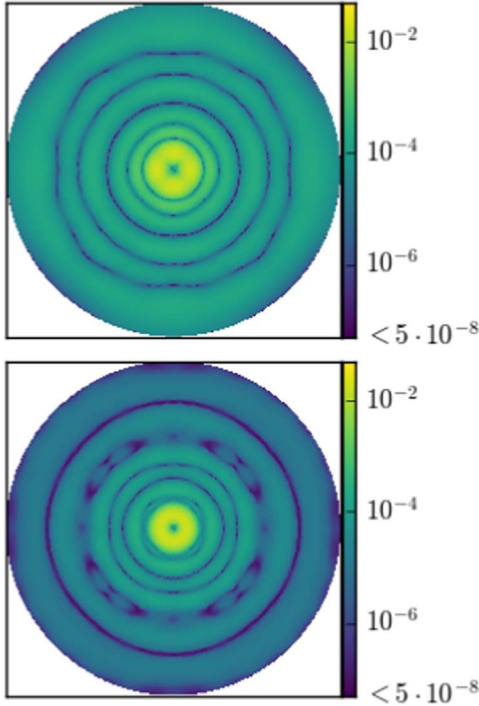


Figure 2. Magnitude of the linear polarization leakage beam given by $\mathcal{M}_p = \sqrt{\mathcal{M}_{IQ}^2 + \mathcal{M}_{IU}^2}$, or the middle two entries of the top row of Figure 1, at 120 MHz and 160 MHz (above and below, respectively).

3. $V^I \rightarrow V^V$ occurs through the difference in D -terms between two feeds.

We detail how we obtain the direction-independent Jones terms in the next section.

3. Observations and Reduction

In this work we used eight nights of observations from the HERA-19 commissioning array. HERA is a low-frequency

interferometer composed of 14 m-diameter dishes arranged in a close-packed hexagonal array of 14.7 m spacing. The commissioning array consists of 19 dishes (see Figure 3); HERA is being constructed in staged build-outs and upon completion will consist of 350 dishes in a fractured hexagon configuration (see Dillon & Parsons 2016; DeBoer et al. 2017). A feed cage containing two dipole feeds (recycled from the PAPER array, see Parsons et al. 2010), oriented in the north–south and east–west directions, was suspended above each dish (Ewall-Wice et al. 2016; Neben et al. 2016; Thyagarajan et al. 2016).

HERA only observes in drift-scan mode. The observations we used were eight nights, from Julian Date (JD) 2457548 to 2457555; local sidereal times (LSTs) were 10.5–23 hr. Drift-scan visibilities were recorded every 10.7 s for 1024 evenly spaced channels across the 100–200 MHz bandwidth. These data were divided into MIRIAD data sets roughly 10 minutes long. A night’s observation lasted 12 hr in total (6pm to 6am South African Standard Time; SAST); of these we used the central 10 hr, to avoid the Sun. A summary of the instrument and observation parameters is given in Table 1.

3.1. Radio Frequency Interference (RFI) Excision and Flagging

To identify samples contaminated by RFI, a two-dimensional median filter in time and frequency was applied to the visibility data to smooth out high pixel-to-pixel variations, and remove significant outliers that were likely unphysical. The variance of the resulting data was computed, and points with a z -score greater than 6 (i.e., points where the value is more than 6σ away from the mean) were flagged as initial seeds for RFI extraction. A two-dimensional watershed algorithm was applied using these seeds as starting points, enlarging the regions of RFI-contamination to neighboring pixels with z -scores greater than 2, until all such pixels were flagged. Figure 4 shows the fractional RFI flag occupancy per time (displayed in LST) and frequency across the 8 days of observations. The majority of the band is relatively clear of RFI. Some clear features are: the FM radio band (below

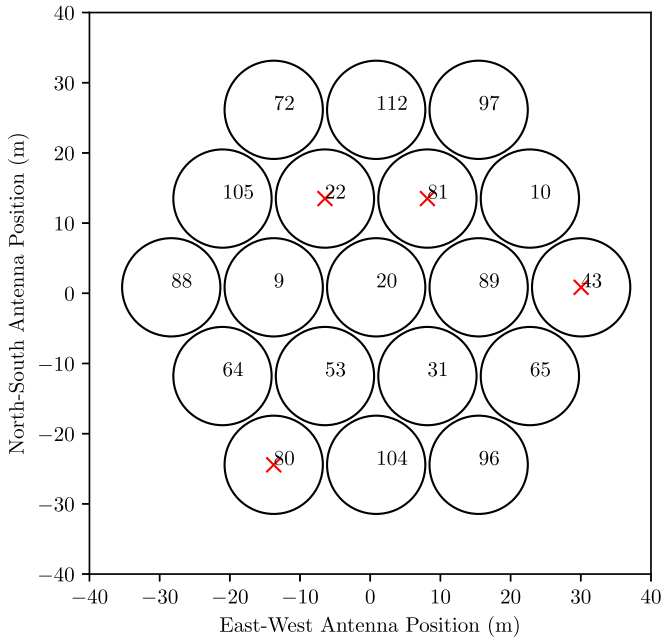


Figure 3. Configuration of the HERA-19 array. The perimeter of each dish is shown as a circle. A red “X” marks antennas that were identified during preprocessing and calibration as malfunctioning and were excluded from further analysis.

Table 1
Observational Parameters Used for This Study

Parameter	Value
Array location	30:43:17.5 S, 21:25:41.9 E
JD range	2457548–2457555
LST Range	10.6–22.6 hr
Frequency range	115–185 MHz
Frequency resolution	97.6 kHz
Integration time	10.7 s
Element diameter	14.0 m
Number of elements	15
Shortest baseline	14.6 m
Longest baseline	58.4 m
At 150 MHz:	
Primary beam FWHM	9°
Synthesized beam FWHM	2°
SEFD per element	~5800 Jy

110 MHz), ORBCOMM satellite communications (137 MHz), an ISS downlink (150 MHz), and VHF TV channels (above 170 MHz).³⁶ The galaxy, when transiting zenith at LST ≈ 17.75 hr, is so bright that it appears to degrade our ability to flag RFI.

Four antennas were identified during the commissioning as having anomalous behavior. These are marked with red “X”s in Figure 3 and were omitted from further analysis. Before calibration, we manually flagged the edges of the band (below 110 MHz and above 190 MHz), where spectral behavior is dominated by the high and low pass filtering in the HERA signal chain (DeBoer et al. 2017).

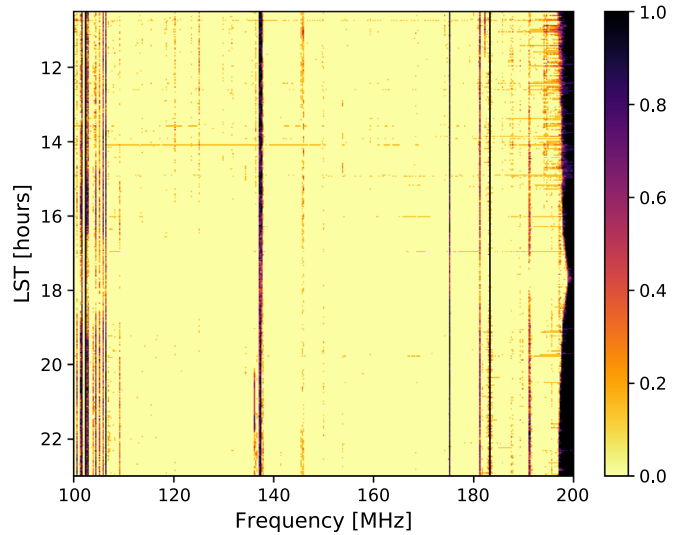


Figure 4. Fractional RFI flag occupancy per time and frequency over the eight days of observations. RFI was flagged on a per-(time,frequency) sample basis.

3.2. Calibration

HERA is designed to be calibrated using redundant calibration techniques (Dillon & Parsons 2016), but for this preliminary view of HERA commissioning data, we used image-based calibration. Future studies with deeper integrations targeting EoR detections will take advantage of redundancy to obtain more precise calibration solutions (DeBoer et al. 2017). We used the CASA (McMullin et al. 2007) package for calibration, taking advantage of its CLEAN, gaincal and bandpass functions. We first converted from HERA’s native MIRIAD to a UVFITS file format using PYUVDATA (Hazelton et al. 2017); this could then be ingested by CASA.

The brightest calibration sources near the decl. -30° stripe—for example, those used in previous PAPER analyses like Pictor A (Jacobs et al. 2013)—were not available for this observing window (10.5–23 hr R.A.), and the few long baselines in the array available made calibration using individual fainter point sources difficult. We therefore developed a calibration method using the Galactic Center (GC; taken to be at $\alpha, \delta = 17^h 45^m 40^s, -29^\circ 0' 28''$) as modeled by the GSM. Specifically, we selected four minutes of data centered at the transit of the GC to use for calibration. The visibilities were phased from drift-scan mode to a single phase-center chosen to be the LST at the start of the observations. Because this phasing imperfectly approximates the tracking telescope assumed by CASA, the length of the observation was chosen to minimize the effects of beam-dependent gain variations as the GC transited. The calibration was done as a two-step process. First, we built an initial model with the GC as an unpolarized, flat-spectrum source with flux density scaled to a reference point of 1 Jy. This allowed us to solve for the large antenna-based delay terms using gaincal (gaintype=’K’; typically tens of nanoseconds) and a complex bandpass using bandpass. A single solution was obtained for the 4 minute observation file for both calibration types, and for the bandpass solution a solution was obtained for each unflagged ~ 100 kHz channel, resulting in a complex, frequency-dependent gain for each feed. With this first calibration in place, the second step was to interactively CLEAN the image to obtain a more accurate model of the GC

³⁶ For an extended discussion of RFI as seen by HERA, see the public HERA Memo #19 (http://reionization.org/wp-content/uploads/2013/03/HERAMemo19_HERA_dish_RFI.pdf).

extended structure. We still assumed an unpolarized source, but allowed multiple components within a two degree radius centered on the GC. This was followed by a second round of delay and bandpass calibration to the multi-component extended model, completely analogous to the first round of calibration. At this point, an overall frequency-dependent amplitude was required to scale the gains from the arbitrary 1 Jy normalization. For this we used our simulation of the GC from the GSM (converted to units of Jy) to determine a single, spectrally smooth function for all antennas to make the spectrum of the observations match the simulations.

Clearly, this is an incomplete calibration model. The assumption that the GC is unpolarized is probably adequate, due to the large optical depth toward the GC (Oppermann et al. 2012), resulting in near-complete depolarization in the plane of the Galaxy (Wolleben et al. 2006). Moreover, we expect significant beam depolarization due to the large solid angle of the synthesized beam (see Table 1). Other assumptions are less obviously correct. The GC structure is only partially modeled, and we have assumed the GSM provides an accurate calibration. We have also assumed that the direction-independent Jones matrix is diagonal. Although in principal CASA is capable of solving for D -terms using the `polcal` task, we did not find that the solutions obtained using only an unpolarized GC model were stable or improved the image quality. The lack of polarized point sources as calibrators limits our interpretive power for addressing some aspects of polarization leakage, which we discuss in Section 4.

The calibration we have obtained serves to correct an initial large cable delay per antenna, which aligns all of the power spectra at zero delay, and sets the overall flux scale. The resulting complex antenna-based gains are shown in Figure 5. The gain amplitudes are clearly very similar in shape, with one outlier, and they cluster with 25% of each other. After removing the phase due to the delay term, the resulting phases show only small variations around their mean. The derived bandpasses are clearly spectrally smooth, and thus, even if there are errors, we expect that they will not add additional spectral structure to the power spectrum (see Section 3.3). These gains were applied to all 8 nights of observations. It was found that this produced smaller day-to-day calibration variability than calibrating each day separately to the GC. An estimate of the remaining variation is discussed in Section 4.3.

Figure 6 shows the effect of calibration on the visibilities of three nominally redundantly spaced baselines. Shown in that figure are the phases of three V^m visibilities from 14.7 m baselines before and after calibration. There were no shared antennas between the visibilities shown. The qualitative agreement is obvious, providing a consistency check on the solutions, and showing our sky-based model achieves redundancy without assuming it. However, small-scale variations between baselines are still seen. This not unexpected; the antennas are likely to be non-identical, and we have evidence based on closure phase (which is insensitive to calibration errors) that redundant baselines do not see the sky identically (Carilli et al. 2018).

In Figure 7, we show images formed from the simulated pseudo-Stokes visibilities (top panels) and our observations (bottom panels). These are multi-frequency synthesis images, where we used all unflagged frequencies on either side of the band edges, from 115 to 188 MHz. The primary beam has not

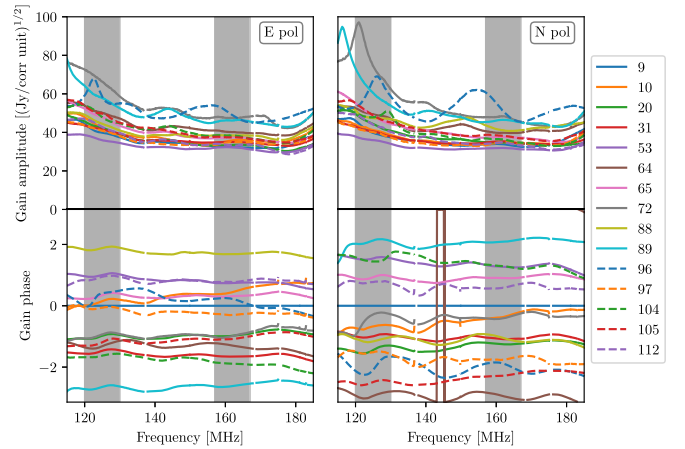


Figure 5. Bandpass solutions obtained for both dipole orientations for all functioning antennas in the array on JD 2457548, and subsequently applied to all data. Each antenna is marked by a different line color and style. Shaded regions indicate the effective sub-bands (the 10 MHz at the center of the 20 MHz Blackman–Harris window) used for power-spectrum analysis. The phase is shown after the removal of the delay term.

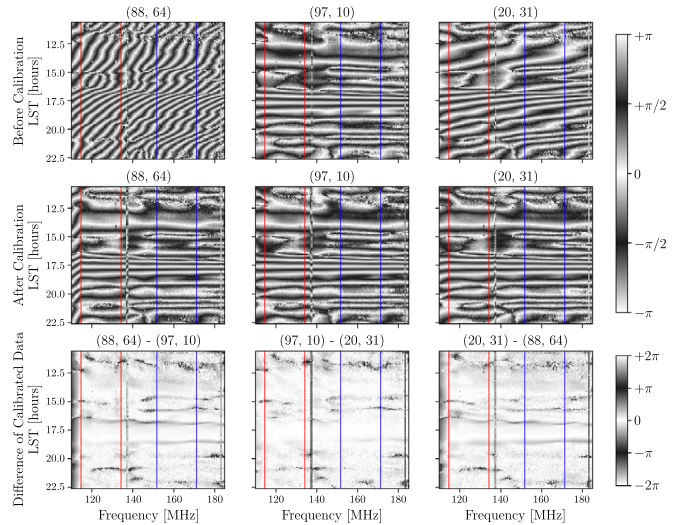


Figure 6. Effect of calibration on the phases of visibilities from three redundantly spaced 14.7 m baselines; mn polarization. The antenna numbers refer to those given in Figure 3. The color scale is cyclic; black is $\pm\pi/2$ and white is 0 and $\pm\pi$. The extent of the low band is indicated with red lines and the high band is shown with blue lines. Top row: before calibration. Middle row: after calibration. Bottom row: the three pairs of differences of the calibrated phases. Note that the agreement between baselines is excellent near the Galactic Center but shows significant differences at some other times.

been deconvolved. All images shown were produced using the same four-minute interval used for calibration. Note that at HERA’s latitude the GC transits 2° north of zenith, while the HERA primary beam has a FWHM of $\sim 10^\circ$ at 150 MHz (Neben et al. 2016). For the simulated visibilities, we flagged the same antennas and channels as in the data. As expected for a compact array, the Stokes I images capture only a low-resolution view of the GC. The simulated and observed visibilities form remarkably similar images in Stokes I , and Q and U clearly share features in common, due to leakage from I to Q and U through the primary beam (recall that the simulations are unpolarized). In Stokes V , the simulated map

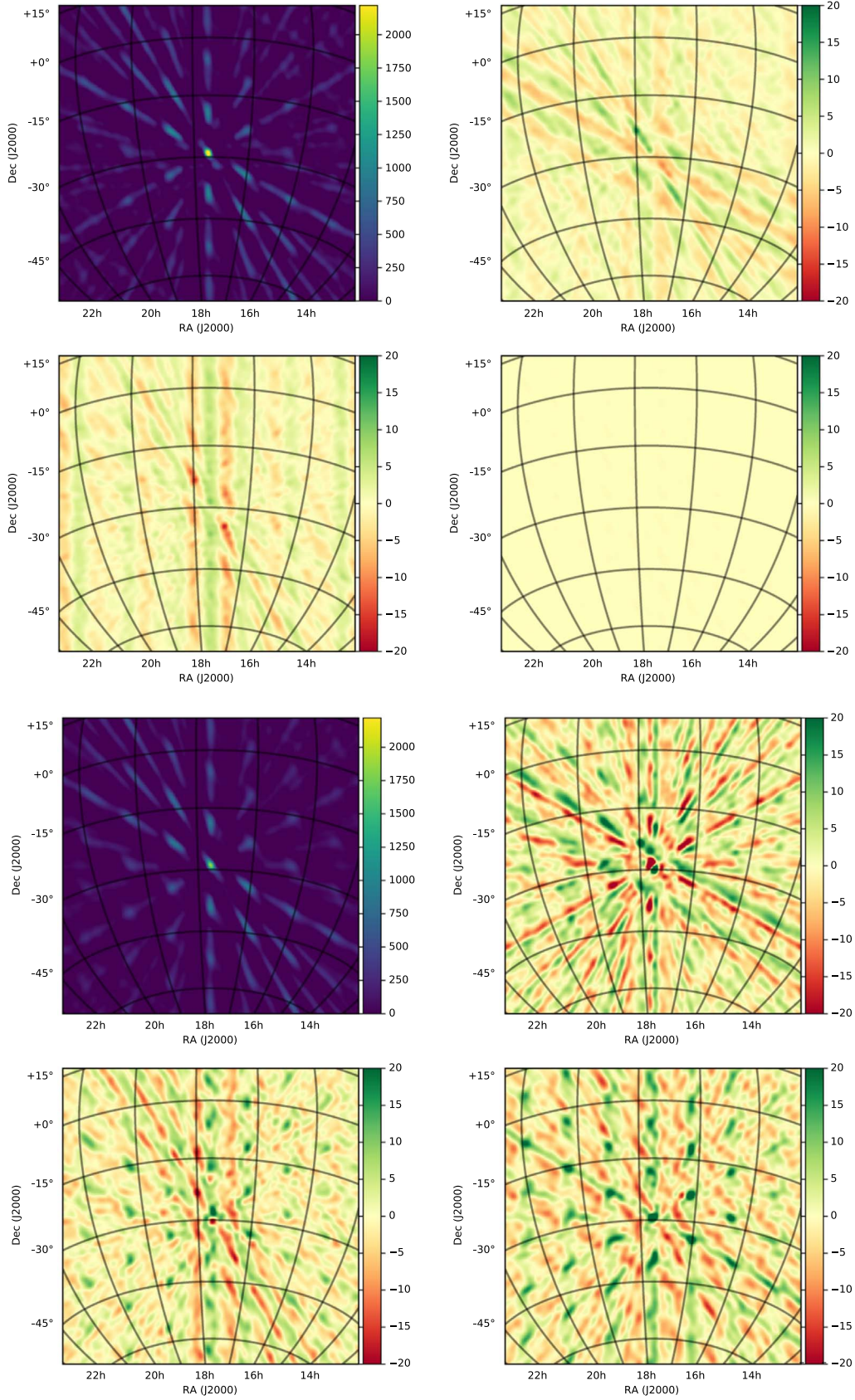


Figure 7. Both sets of panels show multi-frequency synthesis pseudo-Stokes images of I , Q , U , and V visibilities (top left, top right, lower left, lower right) for the Galactic Center (our calibration source) at transit. Note the field-of-view shown is about 60° across. A Briggs-weighting with robustness 0 was used when gridding into the image plane. No deconvolution was performed. The color bar is in units of Jy/Beam. A separate color scale is used for Stokes I for a suitable dynamic range in the polarized fluxes; note that the color scales differ by a factor of 100. Above: simulation, where only a Stokes I sky was used. Any polarized power is due to direction-dependent polarization leakage (see Section 2.1). Below: multi-frequency synthesis pseudo-Stokes images formed from observed visibilities on JD 2457548.

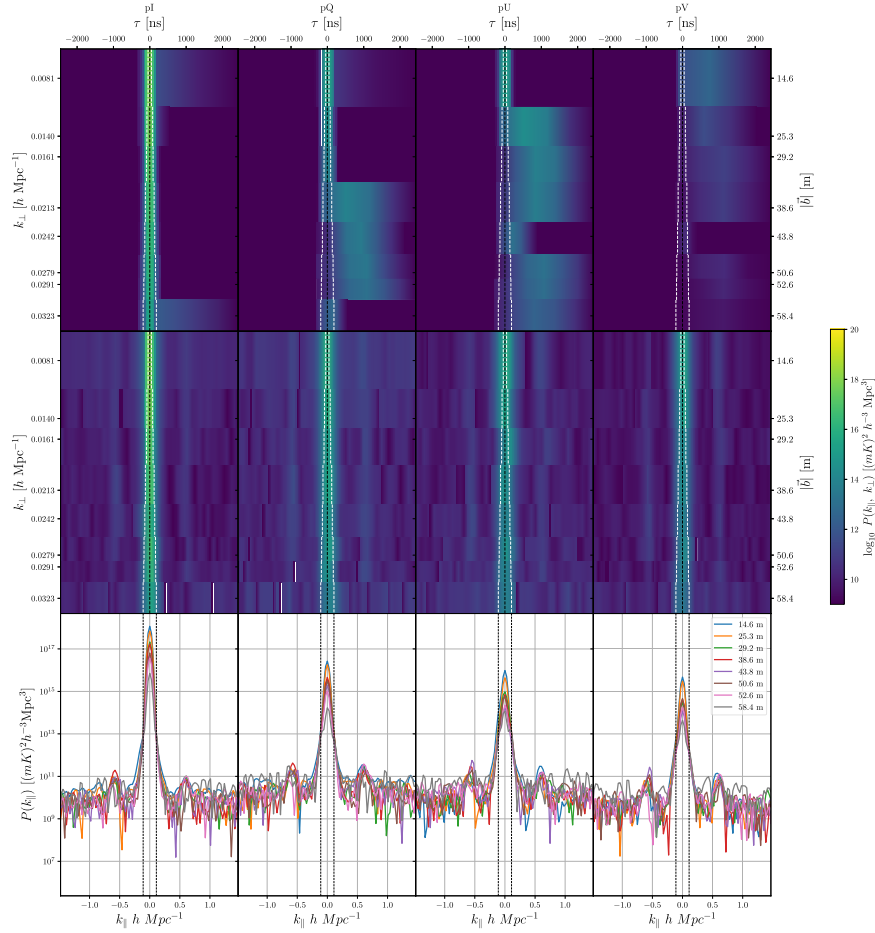


Figure 8. Results from the high band (157–167 MHz). Top: simulated power spectra in Stokes I , Q , U , and V , following the formalism in Section 2. No polarized sky model was used, so power in Stokes Q , U , and V is only due to the direction-dependent beam leakage from Stokes I . No instrumental noise was included in the simulation. Middle: 8 day average power spectra from data. Bottom: the same data as shown in the middle panel, but with each baseline length overlaid to allow shared features to be more easily identified. For the top and middle plots, the white dotted lines indicate the boundary of the pitchfork and the EoR window for that baseline length. A black dotted line indicates the $k_{\parallel} = 0 \text{ h Mpc}^{-1}$ line. In the bottom panel, dotted lines indicate the boundary of the wedge for the longest baseline only. Delays in nanoseconds are indicated along the top, and the corresponding cosmological k at the mean redshift along the bottom axis.

has a significantly smaller amplitude of features compared to the actual image generated from data. The presence of emission at the location of the Galactic Center not due to primary beam leakage is consistent with direction-independent gain errors at the few percent level in amplitude (for Stokes Q) and D-terms at $\sim 1\%$ relative to the diagonal gains (for Stokes V) (Thompson et al. 2008). Note that the Stokes U image is broadly consistent with a large fraction of power coming from I leakage through the primary beam, though there is some additional power as well. We consider the implications for the power spectrum in Section 4.

3.3. Forming Power Spectra

Power spectra were formed in a fashion similar to the method used in Pober et al. (2013) and Kohn et al. (2016). The actual implementation of the code is available as part of the GitHub HERA-Team repository `hera_pspec`.³⁷ We briefly review the method here.

Parsons et al. (2012b) defined the delay transform as the Fourier transform of a visibility for baseline ij and pseudo-Stokes

parameter P along the frequency axis

$$\tilde{V}_{ij}^P(\tau, t) = \int d\nu \tilde{V}_{ij}^P(\nu, t) e^{2\pi i \nu \tau}. \quad (11)$$

We selected two relatively RFI-free 20 MHz sub-bands (Figure 4); 115 to 135 MHz and 152 to 172 MHz, henceforth referred to as the “low band” and the “high band,” in which to compute the power spectrum. An extremely conservative cut on RFI was used such that any integration that had RFI flagged in the 20 MHz sub-band was excluded from the analysis. This cut was performed separately for the two bands. In each case, approximately 35% of the data were retained after this cut. The bands were then multiplied by a Blackman–Harris window, centered on their central frequencies, before Fourier transforming, in order to minimize sidelobes. This windowing led to a noise-effective bandwidth of 10 MHz. We note that this bandwidth is appropriate for EoR analyses because the H I signal is, to a reasonable approximation, coeval over the corresponding redshift range (Furlanetto et al. 2006). However, this resolution (approximately 100 ns in delay as compared to 194 ns for the longest baseline in this study) does limit our ability to resolve certain features in the power spectrum. We also note that using a Blackman–Harris window will induce a correlation between adjacent τ modes; this should be kept in mind when interpreting plots, as all delay bins are plotted.

³⁷ https://github.com/HERA-Team/hera_pspec

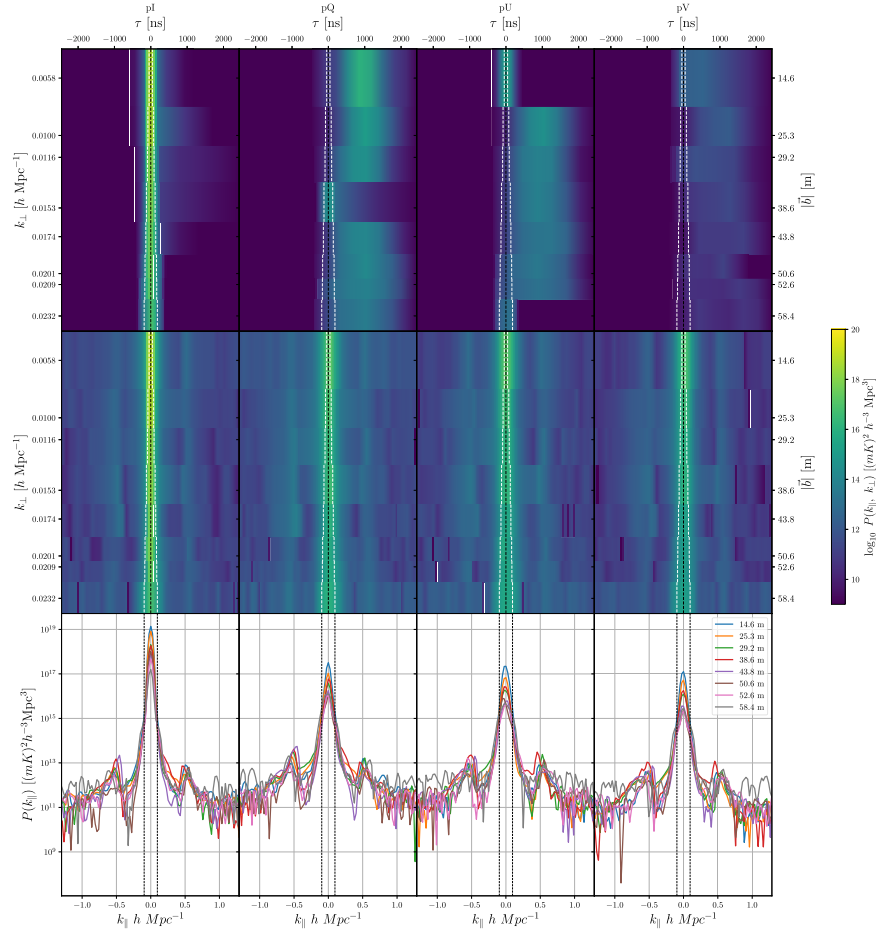


Figure 9. Results from the low band (120–130 MHz), arranged in the same format as Figure 8.

The power at each delay-mode and baseline can be represented in terms of their respective Fourier components k_{\parallel} and k_{\perp} (Parsons et al. 2012b; Thyagarajan et al. 2015a):

$$P(k_{\parallel}, k_{\perp}) \approx |\tilde{V}_{ij}^P(\tau)|^2 \frac{X^2 Y}{\Omega_{pp} B_{pp}} \left(\frac{c^2}{2k_B \nu^2} \right)^2, \quad (12)$$

$$k_{\parallel} = \frac{2\pi \nu_{21\text{cm}} H(z)}{c(1+z)^2} \tau,$$

$$k_{\perp} = \frac{2\pi}{D(z)\lambda} b$$

for: cosmological bandwidth B_{pp} and cosmological angular area of the beam Ω_{pp} , $\nu_{21\text{cm}} \approx 1420$ MHz, baseline length b , wavelength of observation λ , Hubble parameter $H(z)$, transverse comoving distance $D(z)$, and redshift-dependent scalars X and Y (Parsons et al. 2012a). Note that the angular area of the beam refers to the diagonal components of the Mueller matrices shown in Figure 1. For further discussion of forming polarized power spectra in k -space, refer to Nunhokee et al. (2017).

To avoid a noise bias when forming the power spectrum, we cross-multiplied consecutive integrations (each having independent noise), rephasing the zenith angle of the latter to the former:

$$|\tilde{V}_{ij}^P(\tau, t)|^2 \approx |\tilde{V}_{ij}^P(\tau, t) \times \tilde{V}_{ij}^P(\tau, t + \Delta t) e^{i\theta_{ij, \text{zen}}(\Delta t)}|, \quad (13)$$

where $\theta_{ij, \text{zen}}(\Delta t)$ was the appropriate phasing for baseline ij and $\Delta t = 10.7$ s.

Pseudo-stokes power spectra were formed for each pair of integrations, for every baseline, according to Equation (13). Power spectra from baselines of identical lengths were then averaged together for all observation times over 8 days. The resulting “1D” power spectra for each baseline length were then concatenated to form a two-dimensional power spectrum (that is, arranged into the $(k_{\perp}, k_{\parallel})$ plane). Note that all averaging in this study was performed after forming power spectra, not by averaging visibilities; this incoherent averaging is non-optimal for achieving the greatest sensitivity. Future work will be able to test the features of the polarized beam and foregrounds to much greater depth.

4. Results

The power spectra formed from the above procedure are shown for all pseudo-Stokes parameters for the high and low bands in Figures 8 and 9, respectively.

4.1. General Features of the Power Spectra

Several features of the power spectra are readily apparent. The first is that foreground emission appears in a relatively narrow band near $k_{\parallel} = 0$. Another is that the shape of the power spectrum as a function of k_{\parallel} is both sharply peaked and relatively featureless. We note that in a similar study of 2D

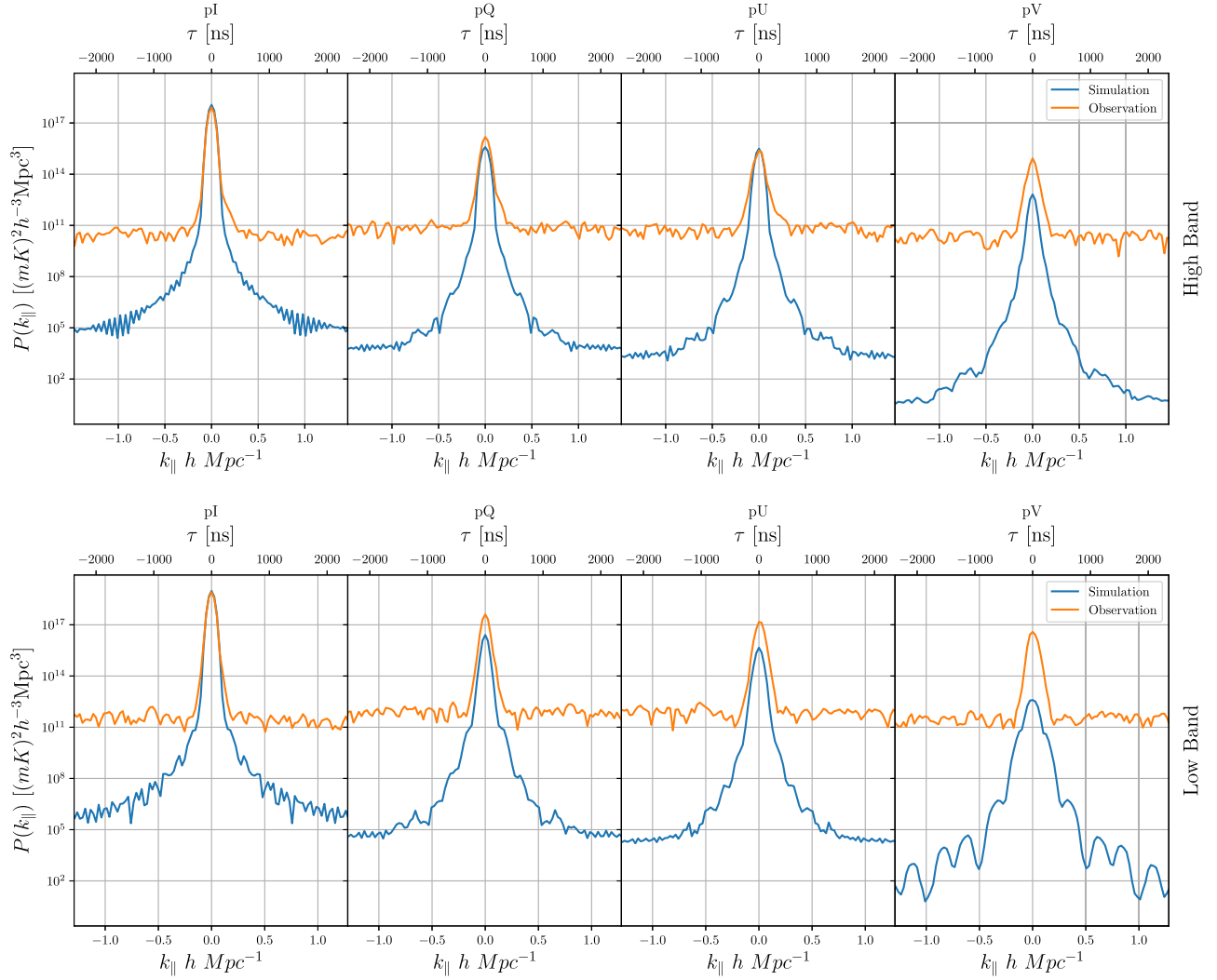


Figure 10. Simulated and observed power as a function of k_{\parallel} for the shortest baseline (14.6 m). Left to right: pseudo-Stokes I , Q , U , and V . Above: the high band. Below: the low band. The simulations were noiseless and used an unpolarized sky model. The agreement with Stokes I is excellent in the high band, and consistent with an absolute calibration accuracy of $\sim 20\%$ for the low band. The agreement between the simulations and the data for the other pseudo-Stokes parameters is poor, as discussed in the text, likely due to a combination of calibration errors, particularly for Stokes V , and actual polarized emission.

polarized power spectra in Kohn et al. (2016), PAPER measurements showed a comparably “filled” region of Fourier space out to the horizon delay (i.e., to directions corresponding to zenith angle $\pm 90^\circ$), with some supra-horizon leakage (e.g., Pober et al. 2013) into the EoR window itself. The power spectra in Figures 8 and 9 show similar behavior, though in this case part of the reason is the low resolution (~ 100 ns; see Section 3.3) of the delay transform (Equation (11)) due to the small spectral bandwidth, and the small horizon delay associated with the short baselines of the array. Thus, we are not able to verify the prediction of Thyagarajan et al. (2015a) and Neben et al. (2016) that for dishes such as HERA, the region between a delay of about 50 ns (set by the width of the antenna primary beam) and the horizon should be free of foreground emission. Similarly, an “excess” of power near the horizon delay, as predicted by the same authors, is not observable, again due to the blurring of features in k_{\parallel} by the resolution. Along the k_{\perp} direction in Stokes I , the amplitude declines as a function of k_{\perp} , as expected for diffuse Galactic emission with a power-law angular power spectrum (larger fluctuation power on large scales). This trend is also observed for the other Stokes parameters as well.

A notable feature in the observational data is a peak in power above the noise level at a delay of ~ 1000 ns, independent of the baseline length or the frequency band. There are ~ 150 m coaxial cables connecting the HERA dishes to the correlator³⁸ and we have evidence that some of this power is due to a cable reflection at this stage of the signal chain producing an alias of the foreground signal; see HERA Memo #39³⁹ (Ewall-Wice 2017). However, this signal should appear at a delay corresponding to 1300 ns, or twice the propagation time in the coaxial cable. It appears that most of the signal present here is present at a smaller delay, and its origin is not understood.

4.2. Comparison to Simulations

In Figure 10, we show a direct comparison between the power spectra of the data and the simulations for the shortest

³⁸ This stage of the signal chain is only present in the commissioning array. Future HERA build-outs will transition to a different architecture using RF over fiber with very long cable lengths to move this signal to even longer delays (DeBoer et al. 2017).

³⁹ http://reionization.org/wp-content/uploads/2013/03/HERA39_H1C_cable_reflections_ewall-wice.pdf

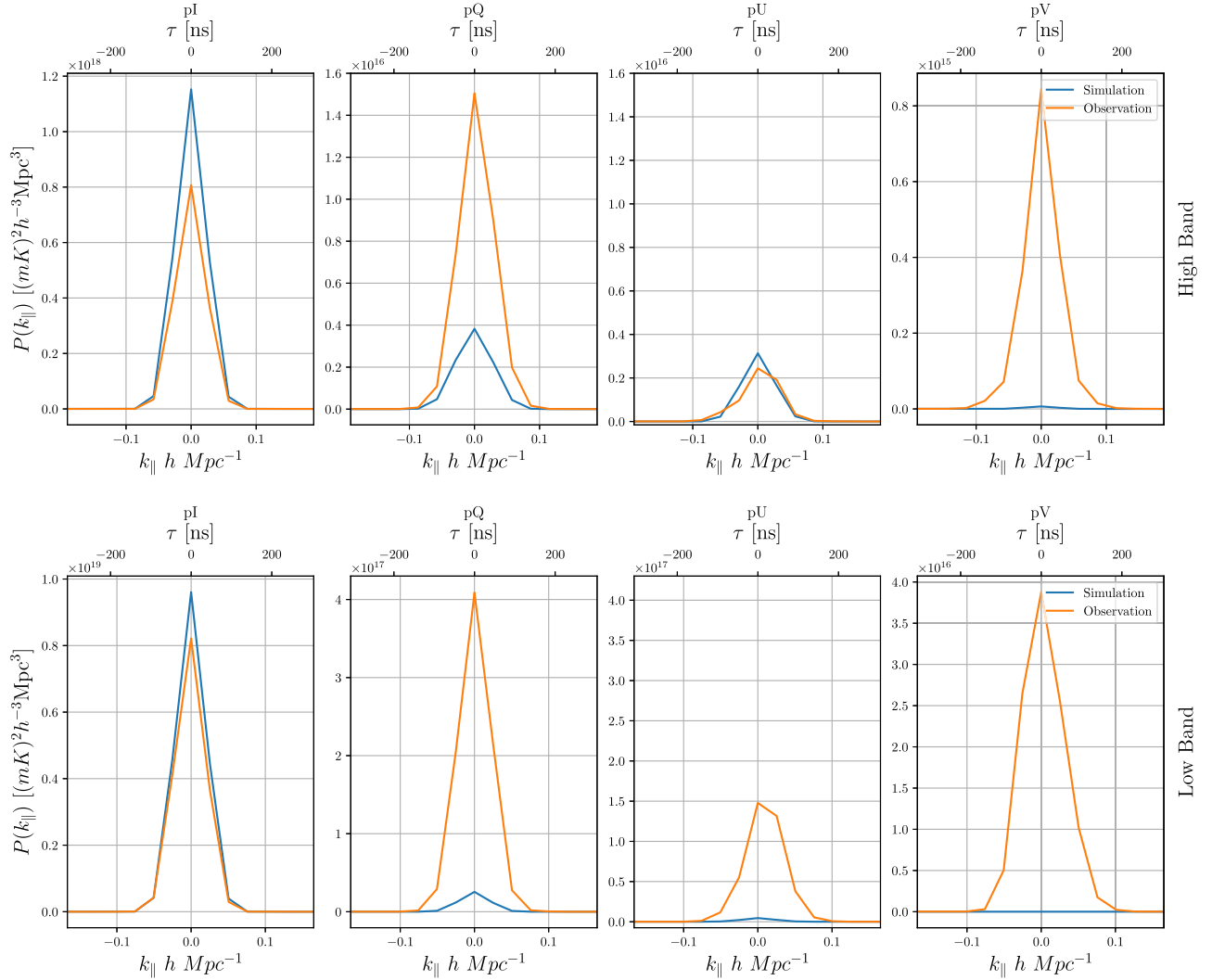


Figure 11. Zoom on Figure 10 showing just the k_{\parallel} values near the wedge, and with a linear scale in $P(k_{\parallel})$. Note that the scale changes for each parameter, except Q and U are set to have the same scale in each row.

baseline length for all Stokes parameters for both bands. Figure 11 shows a zoom of the same data close to the wedge. Recall that the simulations include only a Stokes I sky component and no simulated calibration errors, so the signal in the simulated pseudo-Stokes Q , U , and V power spectra is due solely to wide-field beam leakage (Figure 1). The Stokes I model is the diffuse emission of the GSM, which should be accurate at the scales probed by a 14.7 m baseline, as the model includes scales down to 1° . The power spectra of the simulated data have been computed in the same way as the data.

In comparing to the foreground simulations, there are two things to notice. The first is the isolation, or the degree to which the foregrounds remain within the range of k_{\parallel} defined by their intrinsic smoothness and by the mode-mixing of the interferometer, and which can be characterized by the width of the foregrounds in k_{\parallel} (or τ) space. The second is the dynamic range, defined here as the ratio between the $k_{\parallel} = 0$ peak and the smallest value of the power spectrum. This smallest value may be limited either by noise (in the case of the data) or by the Blackman–Harris window (for the noise-free simulations). We note that the simulations provide a reasonable standard by which to judge both isolation and dynamic range: in the absence of any systematic effects, the width of the foregrounds

in delay space cannot be narrower than that captured by the simulated foreground spectral structure and instrument mode-mixing, and the dynamic range is as expected from the window function. Thus, over a range of about 8 orders of magnitude in the Stokes I power spectrum, limited by the noise in the data, the isolation in the data agrees well with the simulation, arguing that the calibrated data (at the current noise level) do not have significant spectral structure beyond that intrinsically present. It is worth pointing out there is some evidence for broadening of the range in k_{\parallel} near the noise floor. For the other pseudo-Stokes spectra, the isolation is worse: the power spectrum of the data is noticeably wider than the simulation.

Referring to Figure 11, calibrating the raw data to the simulation as described in Section 3.2 reproduces the total power in I very well in the high band, and leads to a total power $\sim 40\%$ higher than the simulation in the low band. This discrepancy is consistent with the overall amplitude of the calibration derived from the GC disagreeing by $\sim 20\%$ in the low band. It is not clear whether this is due to errors in the GSM or the primary beam model at low frequencies. In the analysis that follows, we have increased the amplitude of the simulated power spectrum in the low band to agree with the real data because we are primarily concerned with the relative

power between different pseudo-Stokes parameters; this rescaling allows for a more even treatment of the two bands.

In the high-band analysis, the beam leakage modeled in the simulation is of roughly equal magnitude for both Q and U ; however, the data show a markedly stronger pseudo- Q than U . Because there is no strong reason to believe the sky is highly anisotropic between Q and U over the R.A. included here, this difference argues for another interpretation. The amplitude difference between pseudo- Q and U is $\sim 10\%$ in the visibilities (rather than the power spectra), which can be accounted for by a $\sim 5\%$ relative miscalibration in the antenna-based gain amplitudes between the E and N polarized feeds of the antenna. The pseudo- Q visibilities are constructed by differencing the calibrated nn and ee visibilities, which can make relative amplitude differences between the two polarizations more pronounced. Thus, assuming the excess power in pseudo- Q can be attributed to this difference in gain amplitude between the two polarized feeds, we can use pseudo- U as a measurement of the excess polarized power on the sky not accounted for in the beam leakage from the simulations. This interpretation leads to a combined fractional polarization of $\sim 10\%$. This result is on the high end of the range of measurements of $\sim 1.6\% - 4.5\%$ fractional polarization at 150 MHz on large scales from Jelić et al. (2015) and Lenc et al. (2016). We note that whatever the interpretation of the linear pseudo-Stokes spectra, they do not provide strong evidence for high rotation measure emission, which would be present at $k_{\parallel} > 0.1$ for $RM > 10 \text{ rad m}^{-2}$ in the high band (Moore et al. 2017), although noise prevents probing levels as deep as those in Asad et al. (2018).

As with pseudo- Q and U , pseudo- V has excess power in the measured power spectra compared to the reference simulations. Measurements in the literature do not suggest a significant amount of large-scale circularly polarized emission at the frequencies measured, so this excess power is most likely due to miscalibration of the instrument. Relative phase errors in the gain solutions of the cross-polarized instrumental visibilities can lead pseudo- U to leak into pseudo- V . However, the measured amplitudes of the two power spectra would imply that this systematic error in phase angle must be of order $\pi/2$, or that these phase errors are nearly maximally rotated with respect to the correct value. A more plausible explanation for this excess power in pseudo- V is direction-independent leakage through the D -terms of the Jones matrix, which leak power from pseudo- I (Thompson et al. 2008). As discussed in Section 3.2, D -terms were entirely neglected for the calibration performed in this analysis. Assuming that these D -terms are the source of the leaked power from pseudo- I to pseudo- V , their amplitude relative to the diagonal elements of the Jones matrix would be $\sim 3\%$. This is similar to D -term levels from other low-frequency instruments such as MWA-32, which was found to have $\sim 2\%$ D -terms (G. Bernardi 2019, private communication).

The low-band measurements tell a similar story, with the notable difference that the simulated pseudo- Q and U power spectra exhibit a greater discrepancy than the high-band measurements. This difference may be attributable to the general difficulty of accurately calibrating the low band due to model and beam uncertainties. Performing the same analysis as for the high band, we again find that the inferred polarization fraction from the pseudo- U visibilities is $\sim 10\%$, and the excess power in pseudo- Q can be accounted for by gain amplitude errors of $\sim 5\%$. The relative amplitude of the D -terms to account for the excess power in pseudo- V is closer to 5%,

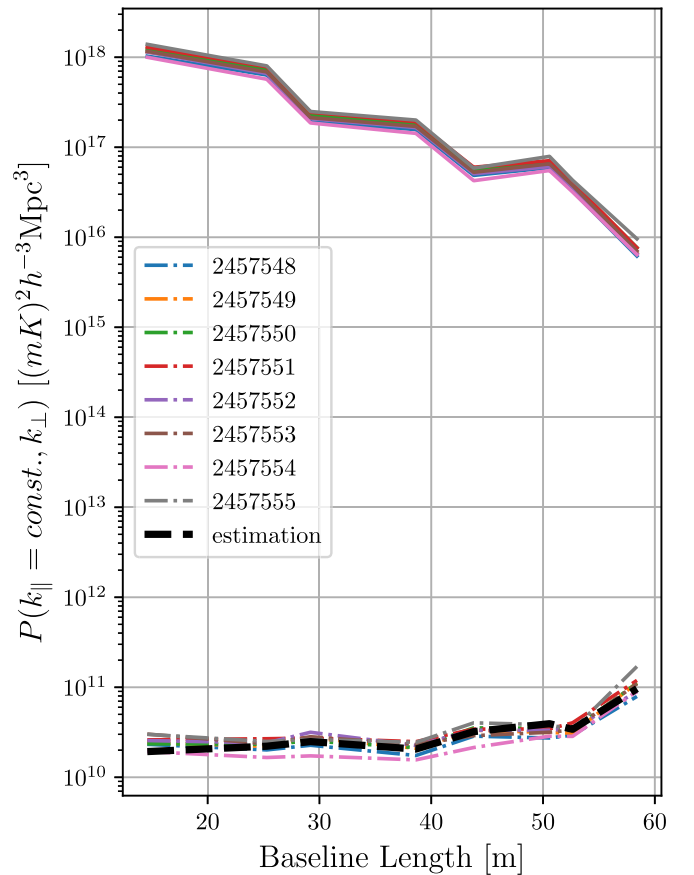


Figure 12. High-band power as a function of baseline length for $k_{\parallel} = 0 \text{ h Mpc}^{-1}$ (solid lines) and an average value over the white noise ($k_{\parallel} > 1 \text{ h Mpc}^{-1}$; dotted-dashed lines) for pseudo-Stokes I on each JD of observation. The black dashed line represents estimated power-spectrum noise given a system temperature of 2400 K. A very similar relationship is seen for the low band (not shown), but with a higher system temperature of 7000 K. Note that the increase of the noise level with baseline length is correctly modeled, as the compact array has a decreasing number of baselines that are averaged together in a given $(k_{\parallel}, k_{\perp})$ bin.

which is slightly higher than the high band but still plausible given the behavior of similar instruments. These results suggest that future precision calibration efforts should include analysis of D -terms in order to accurately model the instrumental effects on the measured visibilities.

4.3. Noise Levels

One estimate of the system temperature of the observations was formed from the calibrated values of the autocorrelations. These were compared against the values obtained from the simulation. Over the R.A. range observed, which was heavily weighted toward the GC and much of the Galactic Plane, the system temperature estimated in this way was 1230 K for the high band and 4000 K for the low band, which was consistent with the simulated autocorrelations (DeBoer et al. 2017, also see the public HERA Memo #16⁴⁰).

The system temperature was converted to a noise level in the power spectrum according to the formalism in Parsons et al. (2012b), with the inclusion of a baseline-number

⁴⁰ http://reionization.org/wp-content/uploads/2017/04/HERA19_Tsys_3April2017.pdf

dependence:

$$P_{\text{Noise}}(k) \approx \frac{1}{2\Delta t \sqrt{N_{\text{LST}} N_{\text{days}} N_{\text{bl}}}} X^2 Y B_{\text{NE}} \Omega_{\text{eff}} T_{\text{sys}}^2, \quad (14)$$

In the above equation, Δt is integration time, N_{LST} is the number of LST hours used per day (12 hr), N_{bl} is the number of baselines (which differed per k_{\perp} bin), X and Y are cosmological scalars defined in Parsons et al. (2012b), B_{NE} is the noise-equivalent bandwidth and Ω_{eff} is the effective beam area, as defined in Parsons et al. (2014). Figure 12 shows power as a function of baseline length for $k_{\parallel} = 0 \text{ h Mpc}^{-1}$ (solid lines) and the average over $|k_{\parallel}| > 1 \text{ h Mpc}^{-1}$ (dotted-dashed lines). Though not shown in Figures 8 and 9, the frequency sampling of the instrument is sensitive to delays up to 5000 ns, and this region defines our white noise level. To match the observed noise level of the power spectrum in Stokes I , the high band required an assumed system temperature of 2400 K, higher than that expected based on the sky and beam model from the simulations, or from the measured calibrated autocorrelations. The cause of this excess is not understood. Figure 12 also shows that both the noise and calibration of the instrument were stable at the 20% level in the visibilities (50% in the power spectrum) over the 8 days presented here.

5. Conclusions

In this work we have investigated the polarization response of the HERA-19 commissioning array, both in imaging and particularly in the power-spectrum domain. We find that a simple image-based calibration based on the unpolarized diffuse emission of the GSM has a spectrally smooth structure and achieves qualitative redundancy between the nominally redundant baselines of the array. We are able to calibrate the data based on the GC observations to the GSM with an accuracy of about 10%, and about 20% variation from day to day.

Forming power spectra in all pseudo-Stokes parameters, we show that we achieve isolation of the foregrounds in Stokes I as expected due to their intrinsic spectral smoothness, the modeled instrument chromaticity, and the calibration, limited in dynamic range by the noise. Excess power at a delay of ~ 1000 ns is seen in all polarizations, which may in part be due to cable reflections, but is not fully explained. Excess power is also seen in the power spectra of the linear polarization Stokes parameters, which is not easily attributable to leakage via the primary beam, and results from some combination of residual calibration errors and actual polarized emission. Finally, Stokes V is found to be highly discrepant from the expectation of zero power, likely due to the lack of calibration of off-diagonal Jones matrix (“ D ”) terms.

The results presented here are necessarily preliminary, and point in obvious directions for improvements in the quality of calibration, particularly the polarized calibration, which are currently being prepared by the HERA collaboration. Deeper integrations in the power spectrum will probe the structure of the foregrounds and instrument response to a higher dynamic range and over a wider range in k_{\perp} -modes as more antennas are added, allowing a more thorough characterization of the wedge shape. A build-out of HERA to 350 antennas with a new broadband feed and completely new electronics chain is now

underway DeBoer et al. (2017), with strong quality-assurance efforts informed in part by this analysis.

This material is based upon work supported by the National Science Foundation under grants No. 1440343 and 1636646, the Gordon and Betty Moore Foundation, and institutional support from the HERA collaboration partners.

HERA is hosted by the South African Radio Astronomy Observatory, which is a facility of the National Research Foundation, an agency of the Department of Science and Technology.

Much of this study was undertaken during the inaugural CAMPARE-HERA Astronomy Minority Partnership (CHAMP), funded under the NSF grants.





S.A.K. is supported by a University of Pennsylvania SAS Dissertation Completion Fellowship. J.E.A. acknowledges support from NSF CAREER award # 1455151. C.D.N. is supported by the SKA SA scholarship program. A.L. acknowledges support from a Natural Sciences and Engineering Research Council of Canada (NSERC) Discovery Grant and a Discovery Launch Supplement, as well as the Canadian Institute for Advanced Research (CIFAR) Azrieli Global Scholar, Gravity and the Extreme universe Program. G.B. acknowledges support from the Royal Society and the Newton Fund under grant NA150184. This work is based on the research supported in part by the National Research Foundation of South Africa (grant No. 103424). J.S.D. acknowledges the support of the NSF AAPF award # 1701536 and the Berkeley Center for Cosmological Physics. M.J.K. is supported by the NSF under project number AST-1613973. Parts of this research were supported by the Australian Research Council Centre of Excellence for All Sky Astrophysics in 3 Dimensions (ASTRO 3D), through project number CE170100013. Computing hardware was provided by funds from the Mt. Cuba Astronomical Foundation.

We thank the anonymous referee for many helpful suggestions.

Software: This research made use of Astropy, a community-developed core Python package for Astronomy (Astropy Collaboration et al. 2013); CASA (McMullin et al. 2007); pyuvdata (Hazelton et al. 2017); pygsm (Price 2016).

ORCID iDs

Saul A. Kohn  <https://orcid.org/0000-0001-6744-5328>
 James E. Aguirre  <https://orcid.org/0000-0002-4810-666X>
 Paul La Plante  <https://orcid.org/0000-0002-4693-0102>
 Chuneeta D. Nunhokee  <https://orcid.org/0000-0002-5445-6586>
 Nicholas S. Kern  <https://orcid.org/0000-0002-8211-1892>
 Adrian Liu  <https://orcid.org/0000-0001-6876-0928>
 Adam P. Beardsley  <https://orcid.org/0000-0001-9428-8233>
 Gianni Bernardi  <https://orcid.org/0000-0002-0916-7443>
 Judd D. Bowman  <https://orcid.org/0000-0002-8475-2036>
 Chris L. Carilli  <https://orcid.org/0000-0001-6647-3861>
 Joshua S. Dillon  <https://orcid.org/0000-0003-3336-9958>
 Aaron Ewall-Wice  <https://orcid.org/0000-0002-0086-7363>
 Steven R. Furlanetto  <https://orcid.org/0000-0002-0658-1243>
 Bryna J. Hazelton  <https://orcid.org/0000-0001-7532-645X>
 Daniel C. Jacobs  <https://orcid.org/0000-0002-0917-2269>
 Matthew Kolopanis  <https://orcid.org/0000-0002-2950-2974>
 Miguel F. Morales  <https://orcid.org/0000-0001-7694-4030>
 Abraham R. Neben  <https://orcid.org/0000-0001-7776-7240>

Nipanjana Patra  <https://orcid.org/0000-0002-9457-1941>
 Max Tegmark  <https://orcid.org/0000-0001-7670-7190>
 Nithyanandan Thyagarajan  <https://orcid.org/0000-0003-1602-7868>
 Peter K. G. Williams  <https://orcid.org/0000-0003-3734-3587>

References

- Asad, K. M. B., Koopmans, L. V. E., Jelić, V., et al. 2015, *MNRAS*, **451**, 3709
 Asad, K. M. B., Koopmans, L. V. E., Jelić, V., et al. 2016, *MNRAS*, **462**, 4482
 Asad, K. M. B., Koopmans, L. V. E., Jelić, V., et al. 2018, *MNRAS*, **476**, 3051
 Astropy Collaboration, Robitaille, T. P., Tollerud, E. J., et al. 2013, *A&A*, **558**, A33
 Bernardi, G., de Bruyn, A. G., Brentjens, M. A., et al. 2009, *A&A*, **500**, 965
 Bernardi, G., de Bruyn, A. G., Harker, G., et al. 2010, *A&A*, **522**, A67
 Bernardi, G., Greenhill, L. J., Mitchell, D. A., et al. 2013, *ApJ*, **771**, 105
 Carilli, C. L., Nikolic, B., Thyagarajan, N., et al. 2018, *RaSc*, **53**, 845
 Carozzi, T. D., & Woan, G. 2009, *MNRAS*, **395**, 1558
 Datta, A., Bowman, J. D., & Carilli, C. L. 2010, *ApJ*, **724**, 526
 de Oliveira-Costa, A., Tegmark, M., Gaensler, B. M., et al. 2008, *MNRAS*, **388**, 247
 DeBoer, D. R., Parsons, A. R., Aguirre, J. E., et al. 2017, *PASP*, **129**, 045001
 Dillon, J. S., Liu, A., Williams, C. L., et al. 2014, *PhRvD*, **89**, 023002
 Dillon, J. S., Neben, A. R., Hewitt, J. N., et al. 2015a, *PhRvD*, **91**, 123011
 Dillon, J. S., & Parsons, A. R. 2016, *ApJ*, **826**, 181
 Dillon, J. S., Tegmark, M., Liu, A., et al. 2015b, *PhRvD*, **91**, 023002
 Ewall-Wice, A. 2017, A Survey of HERA HC1 150m cable reflections, HERA Memo Ser. 39, http://reionization.org/wp-content/uploads/2013/03/HERA39_H1C_cable_reflections_ewall-wice.pdf
 Ewall-Wice, A., Bradley, R., DeBoer, D., et al. 2016, *ApJ*, **831**, 196
 Fagnoni, N., & de Lera Acedo, E. 2016, arXiv:1606.08701
 Farnes, J. S., Gaensler, B. M., & Carretti, E. 2014, *ApJS*, **212**, 15
 Furlanetto, S. R., Oh, S. P., & Briggs, F. H. 2006, *PhR*, **433**, 181
 Geil, P. M., Gaensler, B. M., & Wyithe, J. S. B. 2011, *MNRAS*, **418**, 516
 Hazelton, B., Beardsley, A., Pober, J., et al. 2017, HERA-Team/pyuvdata: Version 1.1, Zenodo, doi:10.5281/zenodo.546260
 Jacobs, D. C., Parsons, A. R., Aguirre, J. E., et al. 2013, *ApJ*, **776**, 108
 Jelić, V., de Bruyn, A. G., Mevius, M., et al. 2014, *A&A*, **568**, A101
 Jelić, V., de Bruyn, A. G., Pandey, V. N., et al. 2015, *A&A*, **583**, A137
 Kohn, S. A., Aguirre, J. E., Nunhokee, C. D., et al. 2016, *ApJ*, **823**, 88
 Lenc, E., Anderson, C. S., Barry, N., et al. 2017, *PASA*, **34**, e040
 Lenc, E., Gaensler, B. M., Sun, X. H., et al. 2016, *ApJ*, **830**, 38
 Liu, A., Parsons, A. R., & Trott, C. M. 2014a, *PhRvD*, **90**, 023018
 Liu, A., Parsons, A. R., & Trott, C. M. 2014b, *PhRvD*, **90**, 023019
 Ludwig, A. 1973, *ITAP*, **21**, 116
 Martinot, Z. E., Aguirre, J. E., Kohn, S. A., & Washington, I. Q. 2018, *ApJ*, **869**, 79
 McMullin, J. P., Waters, B., Schiebel, D., Young, W., & Golap, K. 2007, in ASP Conf. Ser. 376, Astronomical Data Analysis Software and Systems XVI, ed. R. A. Shaw, F. Hill, & D. J. Bell (San Francisco, CA: ASP), **127**
 Mishra, A., & Hirata, C. M. 2018, *PhRvD*, **97**, 103522
 Moore, D. F., Aguirre, J. E., Kohn, S. A., et al. 2017, *ApJ*, **836**, 154
 Moore, D. F., Aguirre, J. E., Parsons, A. R., Jacobs, D. C., & Pober, J. C. 2013, *ApJ*, **769**, 154
 Morales, M. F., Hazelton, B., Sullivan, I., & Beardsley, A. 2012, *ApJ*, **752**, 137
 Neben, A. R., Bradley, R. F., Hewitt, J. N., et al. 2016, *ApJ*, **826**, 199
 Nunhokee, C. D., Bernardi, G., Kohn, S. A., et al. 2017, *ApJ*, **848**, 47
 Oppermann, N., Junklewitz, H., Robbers, G., et al. 2012, *A&A*, **542**, A93
 Parsons, A., Pober, J., McQuinn, M., Jacobs, D., & Aguirre, J. 2012a, *ApJ*, **753**, 81
 Parsons, A. R., Backer, D. C., Foster, G. S., et al. 2010, *AJ*, **139**, 1468
 Parsons, A. R., Liu, A., Aguirre, J. E., et al. 2014, *ApJ*, **788**, 106
 Parsons, A. R., Pober, J. C., Aguirre, J. E., et al. 2012b, *ApJ*, **756**, 165
 Planck Collaboration, Ade, P. A. R., Aghanim, N., et al. 2016, *A&A*, **594**, A13
 Pober, J. C., Liu, A., Dillon, J. S., et al. 2014, *ApJ*, **782**, 66
 Pober, J. C., Parsons, A. R., Aguirre, J. E., et al. 2013, *ApJL*, **768**, L36
 Price, D. C. 2016, PyGSM: Python interface to the Global Sky Model, Astrophysics Source Code Library, ascl:1603.013
 Shaw, J. R., Sigurdson, K., Sitwell, M., Stebbins, A., & Pen, U.-L. 2015, *PhRvD*, **91**, 083514
 Smirnov, O. M. 2011a, *A&A*, **527**, A106
 Smirnov, O. M. 2011b, *A&A*, **527**, A107
 Thompson, A. R., Moran, J. M., & Swenson, G. W., Jr 2008, Interferometry and Synthesis in Radio Astronomy (New York: Wiley)
 Thyagarajan, N., Jacobs, D. C., Bowman, J. D., et al. 2015a, *ApJL*, **807**, L28
 Thyagarajan, N., Jacobs, D. C., Bowman, J. D., et al. 2015b, *ApJ*, **804**, 14
 Thyagarajan, N., Parsons, A. R., DeBoer, D. R., et al. 2016, *ApJ*, **825**, 9
 Thyagarajan, N., Udaya Shankar, N., Subrahmanyam, R., et al. 2013, *ApJ*, **776**, 6
 Trott, C. M., Wayth, R. B., & Tingay, S. J. 2012, *ApJ*, **757**, 101
 van Straten, W., Manchester, R. N., Johnston, S., & Reynolds, J. E. 2010, *PASA*, **27**, 104
 Vedantham, H., Udaya Shankar, N., & Subrahmanyam, R. 2012, *ApJ*, **745**, 176
 Wolleben, M., Landecker, T. L., Reich, W., & Wielebinski, R. 2006, *A&A*, **448**, 411
 Zheng, H., Tegmark, M., Dillon, J. S., et al. 2017, *MNRAS*, **464**, 3486